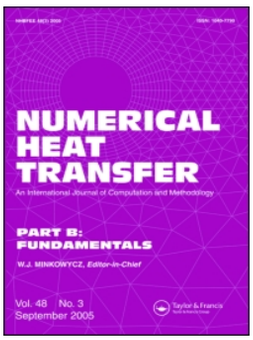

Taylor & Francis
Taylor & Francis Group

Numerical Heat Transfer, Part B: Fundamentals
An International Journal of Computation and Methodology

ISSN: 1040-7790 (Print) 1521-0626 (Online) Journal homepage: http://www.tandfonline.com/loi/unhb20

A fully coupled OpenFOAM® solver for transient incompressible turbulent flows in ALE formulation

L. Mangani, M. Buchmayr, M. Darwish & F. Moukalled

To cite this article: L. Mangani, M. Buchmayr, M. Darwish & F. Moukalled (2017) A fully coupled OpenFOAM® solver for transient incompressible turbulent flows in ALE formulation, Numerical Heat Transfer, Part B: Fundamentals, 71:4, 313-326, DOI: 10.1080/10407790.2017.1293969

To link to this article: http://dx.doi.org/10.1080/10407790.2017.1293969

NUMERICAL HEAT TRANSFER, PART B
2017, VOL. 71, NO. 4, 313–326
http://dx.doi.org/10.1080/10407790.2017.1293969

Taylor & Francis
Taylor & Francis Group

A fully coupled OpenFOAM® solver for transient incompressible turbulent flows in ALE formulation

L. Mangani[a], M. Buchmayr[b], M. Darwish[c], and F. Moukalled[c]

[a]Fluid Section, Hochschule Luzern, Luzern, Switzerland; [b]Department of Tubomachinery, TUGraz, Graz, Austria; [c]Department of Mechanical Engineering, American University of Beirut, Beirut, Lebanon

ABSTRACT

In this article, the previously developed single block fully coupled algorithm [1,2] for solving three-dimensional incompressible turbulent flows is extended to resolve transient flows in multiple rotating reference frames using the arbitrary Lagrange–Euler (ALE) formulation. Details on the discretization of ALE terms along with a recently developed extension to the conservative and fully implicit treatment of multi-block interfaces into three-dimensional space are presented. To account for turbulence, the $k\omega - \text{SST}$ turbulence model in ALE formulation is solved using Navier–Stokes equations. This multi-block transient coupled algorithm is embedded within the OpenFOAM® Computational Fluid Dynamics (CFD) library, and its performance evaluated in a real case involving a turbulent flow field in a swirl generator by comparing numerical predictions with experimental measurements.

ARTICLE HISTORY
Received 11 October 2016
Accepted 20 January 2017

Introduction

In two recent articles [1,2], the authors reported on the development of a fully coupled pressure-based flow solver implemented within the open-source CFD framework OpenFOAM®. Results for a series of test cases demonstrated the advantages of using this combination in simulating complex fluid flow problems [3,4]. The enhancements in efficiency and stability are achieved by resolving the pressure–momentum coupling inherent to the incompressible Navier–Stokes equations in a fully implicit manner [5]. In addition to improved robustness, the solver was shown to scale almost linearly with mesh size, and to require a fraction of the computational time to convergence needed by state-of-the-art segregated flow solvers [6–8] also developed in the OpenFOAM® framework. All test cases dealt with steady-state flow problems in a single reference frame with fixed meshes. In this article, the coupled algorithm is extended to allow for the simulation of transient turbulent flow problems in an arbitrary Lagrange–Euler (ALE) formulation with multiple reference frames, along with a fully implicit and conservative treatment of multi-block interfaces [9,10], denoted by arbitrary mesh interface (AMI). In the AMI algorithm, inter-block interfaces are treated in a fully implicit manner with variables in elements on both sides of the interface implicitly related in their respective algebraic equations. This is critical for ensuring that the high convergence rate and robustness of the basic coupled solver are retained in the solution of these moving AMI configurations. Furthermore, the $k - \omega$ SST turbulence model [11] in ALE formulation is solved to account for sub-grid scale dissipation.

In what follows, the governing equations in ALE formulation are outlined and the fully implicit discretization procedure of the ALE terms is presented. This is followed by a detailed description of the solution procedure. Finally, the transient solver is evaluated by comparing numerical results for the flow field in a swirl generator with experimental measurements.

CONTACT F. Moukalled fmukalled@aub.edu.lb Department of Mechanical Engineering, American University of Beirut, P. O. Box 11-0236, Riad El Solh, Beirut 1107 2020, Lebanon.

Nomenclature

A, *a*	coefficient matrix, coefficient matrix coefficient
ALE	arbitrary Lagrange–Euler
AMI	arbitrary mesh interface
b, *b*	source vector, source vector coefficient
D	Rhie–Chow numerical dissipation tensor
FFT	fast Fourier transform
g	geometric interpolation weighting factor
k	turbulence kinetic energy
MG	measurement gauge
MRF	multiple reference frame
p	pressure
S, *S*	surface normal vector, surface scalar
u, *v*, *w*	velocity components
u	velocity vector
V, $\dot{V}$	volume, volume flux
υ	kinematic viscosity
ρ	density
ω	turbulence frequency

Subscript

C	cell under consideration
eff	refers to effective turbulent viscosity
f	refers to face
g	refers to grid
NB	refers to neighbors of cell C
rel	refers to relative velocity and/or flux

Superscript

u, *v*, *w*	refers to velocity components
¯	linear interpolation to the face

The governing equations

The equations governing incompressible transient flows in the context of an ALE formulation [12] are the continuity and momentum equations given, respectively, by

$$\nabla \cdot \left(\mathbf{u} - \mathbf{u}_g\right) = 0 \tag{1}$$

$$\underbrace{\frac{\partial \mathbf{u}}{\partial t}}_{\text{transient term}} + \underbrace{\nabla \cdot \left[\left(\mathbf{u} - \mathbf{u}_g\right)\mathbf{u}\right]}_{\text{convection term}} = - \underbrace{\frac{1}{\rho}\nabla p}_{\text{pressure term}} + \underbrace{\nabla \cdot \left(\nu_{\text{eff}} \nabla \mathbf{u}\right)}_{\text{diffusion term}} \tag{2}$$

where $\mathbf{u}_g$ is the grid velocity. The laminar kinematic viscosity ν is combined with the turbulent kinematic viscosity ν_t, which accounts for the turbulent stresses arising from the Reynolds-averaged eddy viscosity turbulence model, yielding the effective kinematic viscosity ν_{eff}. The well-known $k - \omega$ shear stress transport model ($k\omega - \text{SST}$) of Menter et al. [11] is used for closure of turbulence quantities. For convenience, the model is written in the following form:

$$\frac{\partial k}{\partial t} + \nabla \cdot \left[\left(\mathbf{u} - \mathbf{u}_g\right)k\right] - \nabla \cdot \left[\left(\nu + \nu_t \alpha_k\right)\nabla k\right] = \frac{1}{\rho} P_k - \beta^* \omega k \tag{3}$$

$$\frac{\partial \omega}{\partial t} + \nabla \cdot \left[\left(\mathbf{u} - \mathbf{u}_g\right)\omega\right] - \nabla \cdot \left[\left(\nu + \nu_t \alpha_\omega\right)\nabla \omega\right] = \frac{\rho C_1 P}{\nu_t} - C_2 \omega^2 + \frac{2\alpha_\varepsilon (1 - F_1)}{\omega} \nabla k \cdot \nabla \omega \tag{4}$$

The discretization process

The fully implicit finite volume discretization of most terms in the governing equations has already been outlined in previous articles [13–16]. The focus here is on discretizing the transient term and the new convective term arising from the use of an ALE reference frame. This is in addition to the extension of the recently developed conservative and fully implicit treatment of multi-block interfaces [9,10] to three-dimensional spaces.

Since the discretization of the governing equations is performed following a finite volume method, the domain is first subdivided into a number of elements. The conservation equations are then integrated over each element and through the use of the divergence theorem, the volume integrals of all fluxes and of the pressure gradient term are subsequently transformed into surface integrals. These integrals are evaluated over the discrete surfaces of the elements and transformed into algebraic equations with their coefficients composed of contributions from the various terms forming the conservation equations. Since in a fully implicit velocity–pressure coupled approach [13–16], the

continuity and momentum equations are solved simultaneously, the system of algebraic equations for every element is written as

$$\begin{bmatrix} a_C^{uu} & a_C^{uv} & a_C^{uw} & a_C^{up} \\ a_C^{vu} & a_C^{vv} & a_C^{vw} & a_C^{vp} \\ a_C^{wu} & a_C^{wv} & a_C^{ww} & a_C^{wp} \\ a_C^{pu} & a_C^{pv} & a_C^{pw} & a_C^{pp} \end{bmatrix} \cdot \begin{bmatrix} u_C \\ v_C \\ w_C \\ p_C \end{bmatrix} + \sum_{F=\mathrm{NB}(C)} \begin{bmatrix} a_F^{uu} & a_F^{uv} & a_F^{uw} & a_F^{up} \\ a_F^{vu} & a_F^{vv} & a_F^{vw} & a_F^{vp} \\ a_F^{wu} & a_F^{wv} & a_F^{ww} & a_F^{wp} \\ a_F^{pu} & a_F^{pv} & a_F^{pw} & a_F^{pp} \end{bmatrix} \cdot \begin{bmatrix} u_F \\ v_F \\ w_F \\ p_F \end{bmatrix} = \begin{bmatrix} b_C^u \\ b_C^v \\ b_C^w \\ b_C^p \end{bmatrix} \tag{5}$$

The block coefficient pattern represents the coefficient matrices needed to implicitly couple the continuity equation with the vectorial momentum equation. The coefficients are composed of influences from the various terms forming the conservation equation. As mentioned earlier, expressions arising from the standard terms were reported in previous articles [1,2] and only contributions from the newly considered terms will be given here. The turbulence model equations are solved sequentially after solving simultaneously the continuity and momentum equations.

Discretization of the transient term

The transient term in Eq. (2) is discretized using the first-order Euler backward scheme, yielding the following implicit and explicit contributions to the coefficients and source terms, respectively:

$$\begin{aligned} a_{C,t}^{uu} &= \tfrac{\Delta V}{\Delta t} \quad b_{C,t}^{u} = \tfrac{\Delta V}{\Delta t} u_{C,t-\Delta t} \\ a_{C,t}^{vv} &= \tfrac{\Delta V}{\Delta t} \quad b_{C,t}^{v} = \tfrac{\Delta V}{\Delta t} v_{C,t-\Delta t} \\ a_{C,t}^{ww} &= \tfrac{\Delta V}{\Delta t} \quad b_{C,t}^{w} = \tfrac{\Delta V}{\Delta t} w_{C,t-\Delta t} \end{aligned} \tag{6}$$

Second-order accurate schemes, such as the Cranck–Nicholson scheme, can be integrated easily to the discretization procedure. However, for the sake of simplicity, the first-order Euler backward method is used here.

Discretization of the ALE convection term

In an ALE reference frame, the convective term in Eq. (2) is linearized by computing the relative volume flux $\left(\dot{V}_{\mathrm{rel,f}} = \mathbf{n} \cdot \left(\mathbf{u}_{\mathrm{f}} - \mathbf{u}_{\mathrm{g,f}}\right) \mathrm{d}S\right)$ using values from the previous iteration. Adopting a first-order upwind discretization, the contributions to the coefficients are obtained as

$$\begin{aligned} a_{\mathrm{C,conv}}^{uu} &= \left\| \dot{V}_{\mathrm{rel,f}}, 0 \right\| \quad a_{\mathrm{F,conv}}^{uu} = -\left\| -\dot{V}_{\mathrm{rel,f}}, 0 \right\| \\ a_{\mathrm{C,conv}}^{vv} &= \left\| \dot{V}_{\mathrm{rel,f}}, 0 \right\| \quad a_{\mathrm{F,conv}}^{vv} = -\left\| -\dot{V}_{\mathrm{rel,f}}, 0 \right\| \\ a_{\mathrm{C,conv}}^{ww} &= \left\| \dot{V}_{\mathrm{rel,f}}, 0 \right\| \quad a_{\mathrm{F,conv}}^{ww} = -\left\| -\dot{V}_{\mathrm{rel,f}}, 0 \right\| \end{aligned} \tag{7}$$

Higher-order Normalized Variable Diagram (NVD) schemes [15,17] may be added explicitly in a deferred correction manner, whereby the upwind cell is always defined by the relative volume flux $\left(\dot{V}_{\mathrm{rel,f}}\right)$ and not by the volume flux in an absolute frame of reference.

Discretization of the continuity equation term

Using the Gauss theorem, the semi-discretized form of the continuity equation in an ALE reference frame can be written as

$$\sum_{\mathrm{f=faces}} \dot{V}_{\mathrm{rel,f}} = 0 \tag{8}$$

The relative volume flux $\left(\dot{V}_{\mathrm{rel,f}}\right)$ is transformed with the aid of the Rhie–Chow velocity interpolation technique [18] into

$$\begin{aligned}\dot{V}_{\mathrm{rel,f}} &= \mathbf{n}\cdot\left(\boxed{\mathbf{u}_{\mathrm{f}}-\mathbf{u}_{\mathrm{g,f}}}\right)\mathrm{d}S \\ &= \mathbf{n}\cdot\left(\boxed{\overline{\mathbf{u}_{\mathrm{f}}}-\overline{\mathbf{D}_{\mathrm{f}}}\left(\nabla p_{\mathrm{f}}-\overline{\nabla p_{\mathrm{f}}}\right)-\mathbf{u}_{\mathrm{g,f}}}\right)\mathrm{d}S\end{aligned} \tag{9}$$

where the expression for the **D** tensor in Eq. (9) is as reported in [1,2]. It can be noticed how the continuity equation conserves the relative fluxes defined as the difference between the absolute flux $\mathbf{u}_{\mathrm{f}}$ and the ALE flux $\mathbf{u}_{\mathrm{g,f}}$ associated with the motion of the mesh. The discretization of the continuity equation follows the same procedure described in [2] with an additional explicit source term arising from its formulation in an ALE reference frame.

The discretization at an arbitrary mesh interface

Arbitrary mesh interfaces are patches that connect adjacent blocks of a mesh. In general, blocks can have patches that do not conformally match their adjacent counterparts on neighboring blocks. For such non-conforming faces (Figure 1), the surface discretization has to account for this overlapping using face fraction weights g_{f}. Recently, Darwish et al. [9,10] reported on a fully implicit treatment of non-matching multi-block interfaces and applied it in two-dimensional spaces. The method is used here and extended into three dimensions. Whereas in two-dimensional problems, the interface connecting two blocks is a line, for three-dimensional meshes it is a plane. To this end, the library available in OpenFOAM® is used to extract the geometric information of overlapping patches. This provides the basic information required to apply the fully implicit conservative method described in Darwish et al. [10]. In effect, the intersection of the overlapping faces is used to define virtual polygonal faces over which the discretization is performed implicitly in a manner that basically stiches the meshes of the two blocks into one discretization matrix as shown in Figure 2.

The surface discretization over these interface faces is carried out over each weighted sub-surface of the respective master surface. The AMI discretization of the pressure gradient term appearing in Eq. (9) is presented next as an example of how a conservative discretization over a weighted sub-surface is carried out. Considering one such sub-surface with a face fraction weight g_{f1}, its

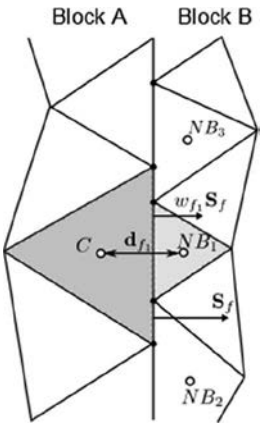

Figure 1. AMI interface. *Note*: AMI, arbitrary mesh interface.

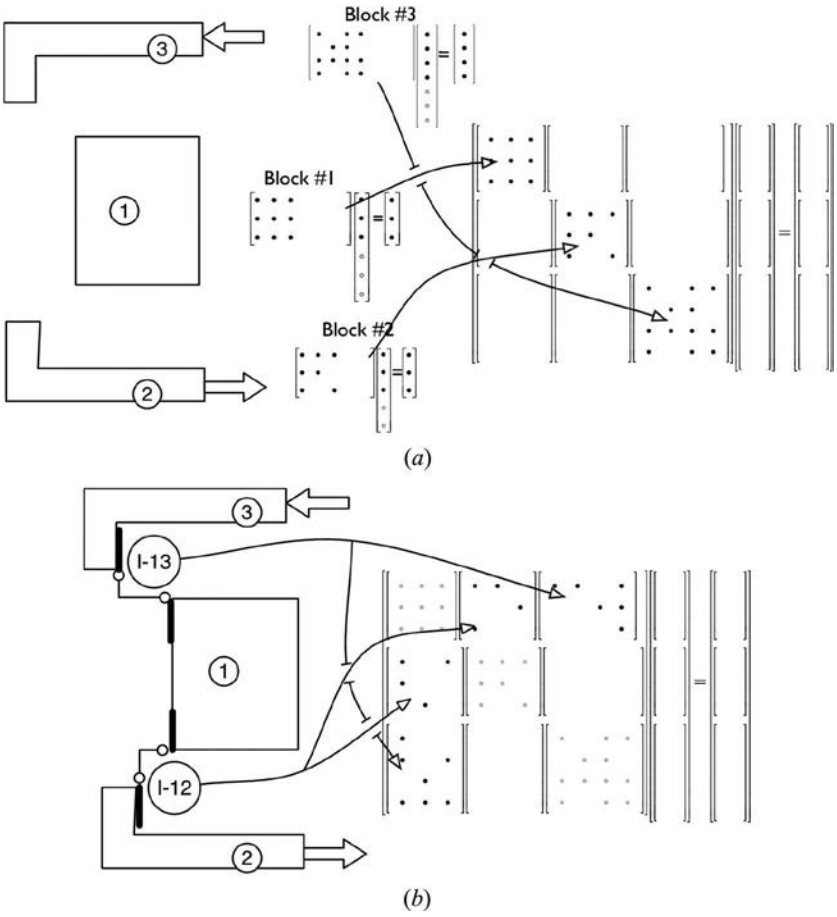

Figure 2. (*a*) Assembly of coefficients arising from the discretization of interior and boundary faces that do not belong to an inter-block patch into local and global matrices (hollow circles are for inter-block connections); (*b*) assembly of coefficients arising from the discretization of interface faces into the global matrix.

discretization is obtained as follows:

$$-g_{f1}\mathbf{S}_f\cdot\bar{D}_f\cdot\nabla p_f=\underbrace{-\frac{|g_{f1}\mathbf{S}_f\cdot\bar{D}_f||g_{f1}\mathbf{S}_f|}{\mathbf{d}_{f1}\cdot g_{f1}\mathbf{S}_f}(p_{F1}-p_C)}_{\text{implicit part}}-\underbrace{\left(g_{f1}\mathbf{S}_f\cdot\bar{D}_f-\frac{|g_{f1}\mathbf{S}_f\cdot\bar{D}_f||g_{f1}\mathbf{S}_f|}{\mathbf{d}_{f1}\cdot g_{f1}\mathbf{S}_f}\mathbf{d}_{f1}\right)\cdot\overline{\nabla p}_f}_{\text{explicit part}} \tag{10}$$

with the meanings of the various terms are as given in [10]. The implicit part, which is the first term on the right-hand side of Eq. (10), is linearized as

$$a_C^{pp}=g_{f1}\frac{|\mathbf{S}_f\cdot\bar{D}_f||\mathbf{S}_f|}{\mathbf{d}_{f1}\cdot\mathbf{S}_f}\qquad a_{F1}^{pp}=-g_{f1}\frac{|\mathbf{S}_f\cdot\bar{D}_f||\mathbf{S}_f|}{\mathbf{d}_{f1}\cdot\mathbf{S}_f} \tag{11}$$

whereas the explicit part is moved to the right-hand side of the algebraic equation.

The discretization at a periodic/cyclic arbitrary mesh interface

The discretization at periodic interfaces is equivalent to connecting two adjacent blocks (although effectively only a patch of a block is connected to another patch of the same block). These periodic interfaces can have also non-conforming faces and can be even cyclic. The discretization procedure of these so-called cyclic AMI follows the same routine as that of an ordinary AMI. However, rotational transformations are necessary to account for the cyclic periodicity.

A sketch of a cyclic AMI interface with rotational periodicity and non-conforming faces is shown in Figure 3. To obtain a conservative implicit discretization for a pair of patches (master and slave), the following steps are performed. First, the centroids of the adjacent cells and the centroids of faces of the adjacent cells of each patch are transformed (rotated). Based on the newly obtained geometric positions, the surface fraction weights g_f are evaluated along with other geometric quantities such as the vector $\mathbf{d}$ connecting two adjacent centroids, distance weights, and surface normal vectors for each neighboring cell pair. Once all geometric entities are processed, the implicit contributions of the various terms in the governing equations to the coefficients are computed. These contributions are conservative since the surface integration is carried out for each face fraction separately. For the momentum equations, this yields a preliminary matrix of coefficients $\mathbf{A}_{\text{geom}}$, which has to be multiplied by a transformation tensor Σ to account for the rotation of the velocity field according to

$$\mathbf{A} = \mathbf{A}_{\text{geom}} \cdot \Sigma \tag{12}$$

For a given pressure–velocity matrix system, the following 4×4 transformation tensor for the neighboring primitive variables ($\mathbf{u}$ and p) is valid in a rotating frame of reference of angular velocity $\mathbf{\Omega}$ with unit rotation vector ω and rotation angle α :

$$\Sigma = \begin{bmatrix} c + \omega_x^2 c_1 & -\omega_z s + \omega_x \omega_y c_1 & \omega_y s + \omega_x \omega_z c_1 & 0 \\ \omega_z s + \omega_x \omega_y c_1 & c + \omega_y^2 c_1 & -\omega_x s + \omega_y \omega_z c_1 & 0 \\ -\omega_y s + \omega_x \omega_z c_1 & \omega_x s + \omega_y \omega_z c_1 & c + \omega_z^2 c_1 & 0 \\ 0 & 0 & 0 & 1 \end{bmatrix} \tag{13}$$

where

$$\begin{aligned} c &= \cos(\alpha) \\ s &= \sin(\alpha) \\ c_1 &= 1 - c \end{aligned} \tag{14}$$

Thus, it can be stated that the coefficient and addressing arrays are "extended" since the coefficients of the cyclic AMI interfaces are added to the coefficient pattern arising from the discretization at internal faces. Injecting the implicit contributions at interfaces directly into the block

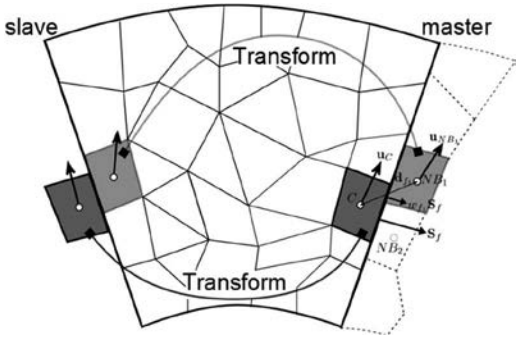

Figure 3. Cyclic AMI interface. *Note*: AMI, arbitrary mesh interface.

matrix structure instead of treating them separately yields some advantages. First, there is no need to create interpolated cyclic AMI interfaces for coarse grid algebraic multi-grid (AMG) levels, which would have been necessary with an explicit treatment at interfaces using a ghost cell approach. In other words, the algebraic agglomeration does not notice any interface, which has a very positive effect on the convergence of the linear solver. Second, the assembly for the direct solver at the coarsest AMG level is also straight forward, since all coefficients are injected into the block matrix and the sparse matrix addressing pattern is known (including that of the injected interface coefficients). Finally, the update of mass fluxes can be carried out by multiplying the solution vector directly by the matrix of coefficients of the continuity equation, avoiding inconsistencies in their reconstruction.

Solution procedure

Following Darwish et al. [13,14], the solution procedure for transient simulations contains an inner loop, in which nonlinear updates of the intermediate fields obtained at a certain time step are carried out, and an outer loop, in which the physical time is increased (Figure 4). After initializing the flow field, the momentum equations are discretized yielding a linearized system of equations. This system is used in constructing the **D** tensor needed in assembling the coefficients of the pressure equation. At that point, the block coupled momentum and pressure equations are solved simultaneously. Then, the turbulence equations are discretized and solved sequentially and the relative volume flux field $\dot{V}_{\mathrm{rel,f}}$ updated. Since many of the coefficients are calculated based on values from the previous iteration, the obtained fields represent values at an intermediate time step between n and $n+1$. Thus, all non-linear and non-orthogonal contributions (convection flux, diffusion flux, sources, and turbulence quantities) need to be updated iteratively. This is accomplished in an inner loop using the solution obtained at the end of any iteration as the initial guess for the following iteration. Computations

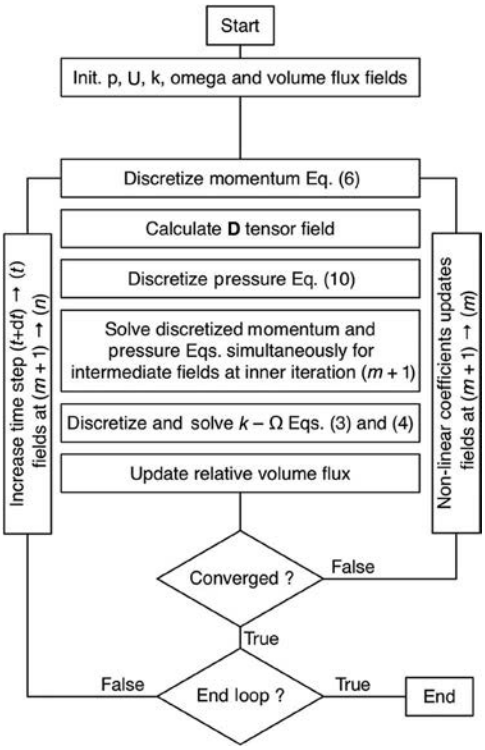

Figure 4. Transient solution procedure for the block coupled solver.

are repeated until changes in the values of variables become negligible indicating that the solution at time step $n + 1$ is reached. Once this is achieved, time is advanced and solution at the new time step is sought (outer loop).

Evaluation

To quantitatively evaluate the presented coupled solver, a swirl generator test case is chosen for which experimental data are available. The test case and experimental measurements were provided by Prof. Susan-Resiga's group from the Polytechnic University of Timisoara, who has done extensive work on swirl generator's setup and flow control [19–21] and has also compared computational results generated using in-house and commercial CFD solvers with measurements [22–24].

In what follows, the newly developed solver will be evaluated by comparing the numerical results of a transient simulation for the flow inside a swirl generator with experimental data. Velocity profiles along sampling lines obtained through Laser Doppler Velocimetry (LDV) measurements are compared with time-averaged numerical results. Moreover, experimental and numerical transient pressure signals at four positions in the flow domains are compared by means of frequency analysis.

Experimental setup

The purpose of setting up a swirl generator loop at the Polytechnic University of Timisoara was to investigate an instability condition in the operation of a Francis turbine. This instability was due to a conical restriction downstream of the turbine runner that led to the occurrence of a large vortex. To investigate the flow physics of this phenomenon, Prof. Susan-Resiga's research group constructed the test loop shown in Figure 5(*a*). The main components of the test rig consist of an inflow duct, guide vanes that lead the flow toward a rotor running in the case of no-load at a speed of 920 rpm and a debit rate of 30 L/*s*. The runner is followed by a convergent nozzle section and a divergent conical section, in which a rope vortex occurs. As shown in Figure 5(*b*), pressure transducers are installed at four levels of this diverging section to extract the main frequencies of the flow. Additionally, LDV measurements have been taken at three positions downstream of the runner [Figure 5(*c*)], one of which in the nozzle section, whereas the other two are located in the divergent conical

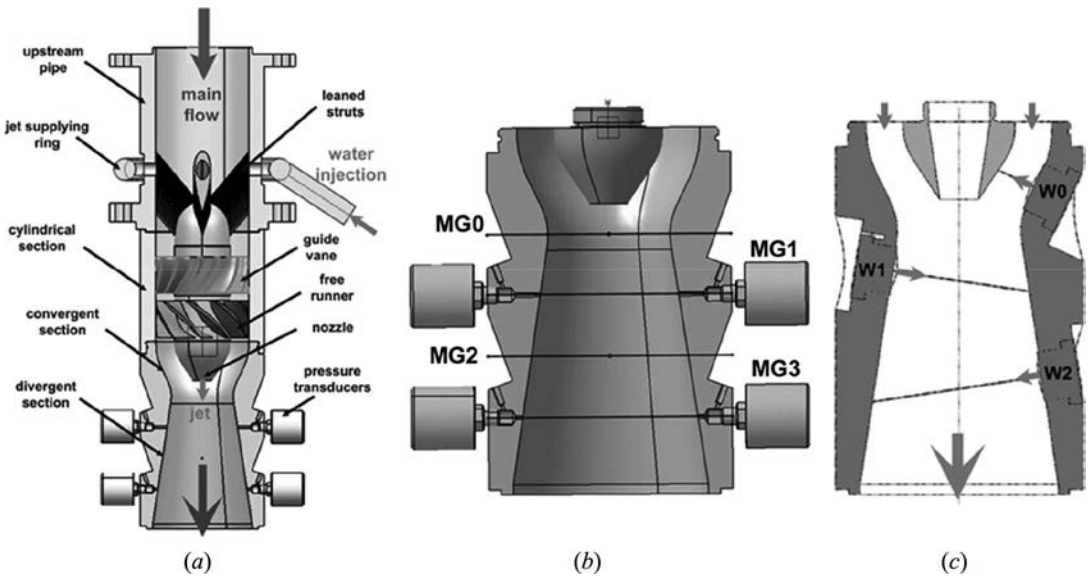

Figure 5. (*a*) Experimental setup of a swirl generator; (*b*) measurement gauge positions; and (*c*) LDV measurement sections [17].

section. Measured velocity profiles and pressure data are used here to validate the newly developed OpenFOAM®-based transient flow solver.

More information about the swirl generator's experimental setup as well as a detailed analytical description of the swirl generator's flow physics is given by Susan-Resiga and Muntean [19], Bosioc et al. [20], and Tanasa et al. [21].

Numerical setup

Corresponding to the experimental setup, a transient simulation with a moving mesh configuration is carried out. The above-described fully coupled transient solver implemented following an ALE formulation including the $k\omega - \text{SST}$ turbulence model is employed. Figure 6 shows the four blocks constituting the numerical calculation domain. The numerical simulation setup approximates the experimental setup with some small differences (e.g., not accounting for the runner blade gaps). The four blocks composing the mesh are separated by AMIs, as outlined above. The discretization at these AMI is implemented in a fully coupled way to guarantee conservativeness of all primitive variables across the non-matching interfaces. At the inlet, the debit rate given above is applied. All static parts of the swirl generator are modeled as no-slip walls. All rotating parts (runner) are modeled as rotating no-slip walls, spinning with the same rotational speed and flow rate as in the experimental setup. At the outlet, a constant pressure boundary condition is prescribed.

These simplistic outlet and inlet conditions impose certain stiffness on the numerical system. This stiffness at the inlet is expected to induce small differences between the numerical and experimental results. A detailed description of the numerical setup is also given by Petit et al. [22].

Results and discussion

A comparison of the numerically computed and experimentally measured time-averaged velocity profiles and pressure frequencies are presented next.

Velocity profiles

As shown in Figure 5(*c*), experimental data of tangential and meridional velocity profiles at the three positions W0, W1, and W2 are available and are compared in Figures 7–9 with numerical results generated using the coupled solver. In these figures, all velocity profiles are normalized by V_{throat} given by

$$V_{\text{throat}} = \frac{Q}{\pi R_{\text{throat}}^2}, \qquad Q = 30 \text{ L/s} \tag{15}$$

and the abscissa by $R_{\text{throat}} = 0.05$ m.

Moreover, prior to comparing results, it should be mentioned that all velocity profiles are similar to those obtained by Petit et al. [22] using a segregated OpenFOAM®-based solver.

The computed meridional velocity profile obtained at section W0 (Figure 7), which lies in the runner section between the hub and shroud [Figure 5(*c*)], is almost on top of the measured one. On the other hand, the absolute tangential velocity profile at the same section is slightly underestimated at the hub side, yielding a smaller integral swirl over the W0 section.

Figure 6. Numerical setup of a swirl generator [19].

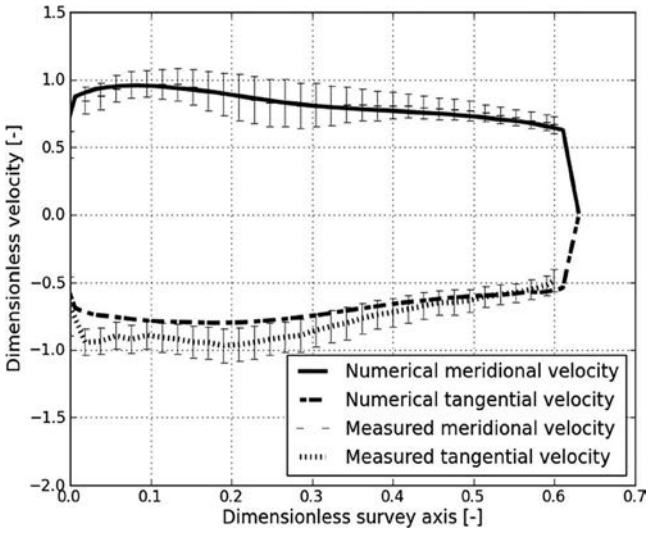

Figure 7. Comparison of the predicted meridional and tangential velocities with LDV measurements at the section W0.

The lower predicted rotational energy at section W0 leads to a slight difference between the predicted and measured meridional velocity at section W1 (Figure 8). As can be seen in Figure 5(*c*), section W1 diagonally crosses the conical diffuser shortly after the end of the runner. Numerical results show a stagnation point halfway between the two sides of the conical diffuser, and as expected a higher meridional velocity is obtained on the right side close to the wall (Figure 8). The underestimation of swirl prevails at section W1, with similar experimental and numerical tangential velocity profiles. The magnitude of the numerical tangential velocity however, consistently remains smaller than the experimental one. Compared to numerical results obtained by Petit et al. [22] with a segregated solver, current results generated using the coupled solver, are closer to measurements. Therefore, the authors believe that section W1 shows a satisfying alignment of measured and calculated velocity profiles.

At the far downstream diverging conical diffuser section W2, the meridional velocity profile displayed in Figure 9 predicts a backflow region in the middle of the diffuser, whereas LDV

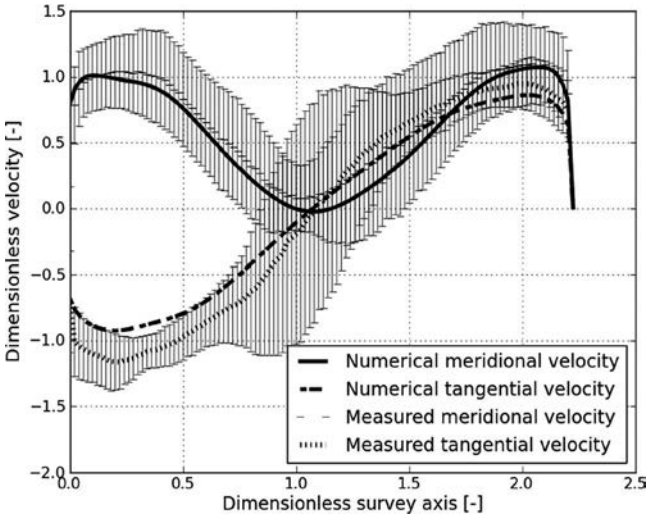

Figure 8. Comparison of the predicted meridional and tangential velocities with LDV measurements at the section W1.

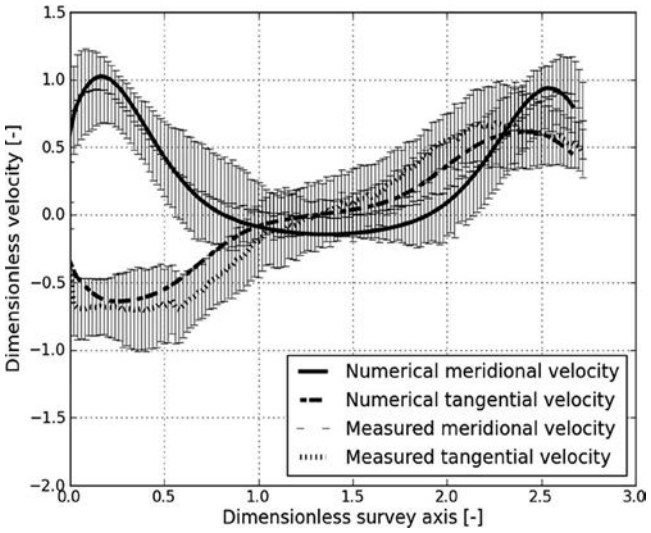

Figure 9. Comparison of the predicted meridional and tangential velocities with LDV measurements at section W2.

measurements yield only a large stagnation zone. Correspondingly, the numerical meridional velocity in the vicinity of the walls is higher than the experimental one.

Concerning the tangential velocity, as for section W1, the shapes of experimental and numerical tangential velocities correspond, with the magnitude of the numerical tangential velocity remaining smaller than the experimental one, which is consistent from a rotational energy point of view.

Finally, by inspecting Figures 7–9, it can be safely stated that the numerical velocity profiles, evaluated at all three sections, remain almost entirely within the error band of LDV measurements.

Pressure frequencies

As shown in Figure 5(*b*), pressure measurements are available at the four positions MG0, MG1, MG2, and MG3 in the conical diffuser part downstream of the runner, where at the given flow rate a vortex rope is established. At these locations, time-dependent samplings of pressure values are performed and to compare magnitudes and frequencies, a fast Fourier transform analysis is carried out, for both measurements and simulations. Figure 10 shows the normalized power spectrum over frequency and provides a comparison between experimental measurements and numerical results at the four measurement gauges (MG) 0 to 3.

Figure 10(*a*) indicates that the main Eigen frequency related to the vortex rope is captured reasonably well by the coupled solver at measurement gauge 0 (MG0). Numerical results correctly reproduce the measured frequency of the vortex rope of 15.5 Hz. This frequency shows that the vortex rope is rotating at the speed of the runner and the numerical simulation is able to reproduce this phenomenon. The shifting in frequency predicted by Petit et al. [22] is not evident in the results reported in Figure 10(*a*). The higher accuracy of the current results can be explained by the adoption in this simulation of the $k\omega - \mathrm{SST}$ turbulence model.

At MG1 [Figure 10(*b*)] and MG2 [Figure 10(*c*)], also the second Eigen frequency is reproduced well. Although the measurements at MG3 [Figure 10(*d*)] is quite noisy, the two main frequencies are also well detected there.

Overall, the comparison shows that numerical and experimental power spectra amplitudes are reasonably close to each other. This means that the vortex rope development is well predicted over its entire length, and numerical predictions reproduce the dynamics of the flow observed experimentally. Moreover, results are somewhat similar (same trend) to those obtained by Petit et al. [22] using a segregated algorithm but closer to measurements in values. Furthermore, results may also be

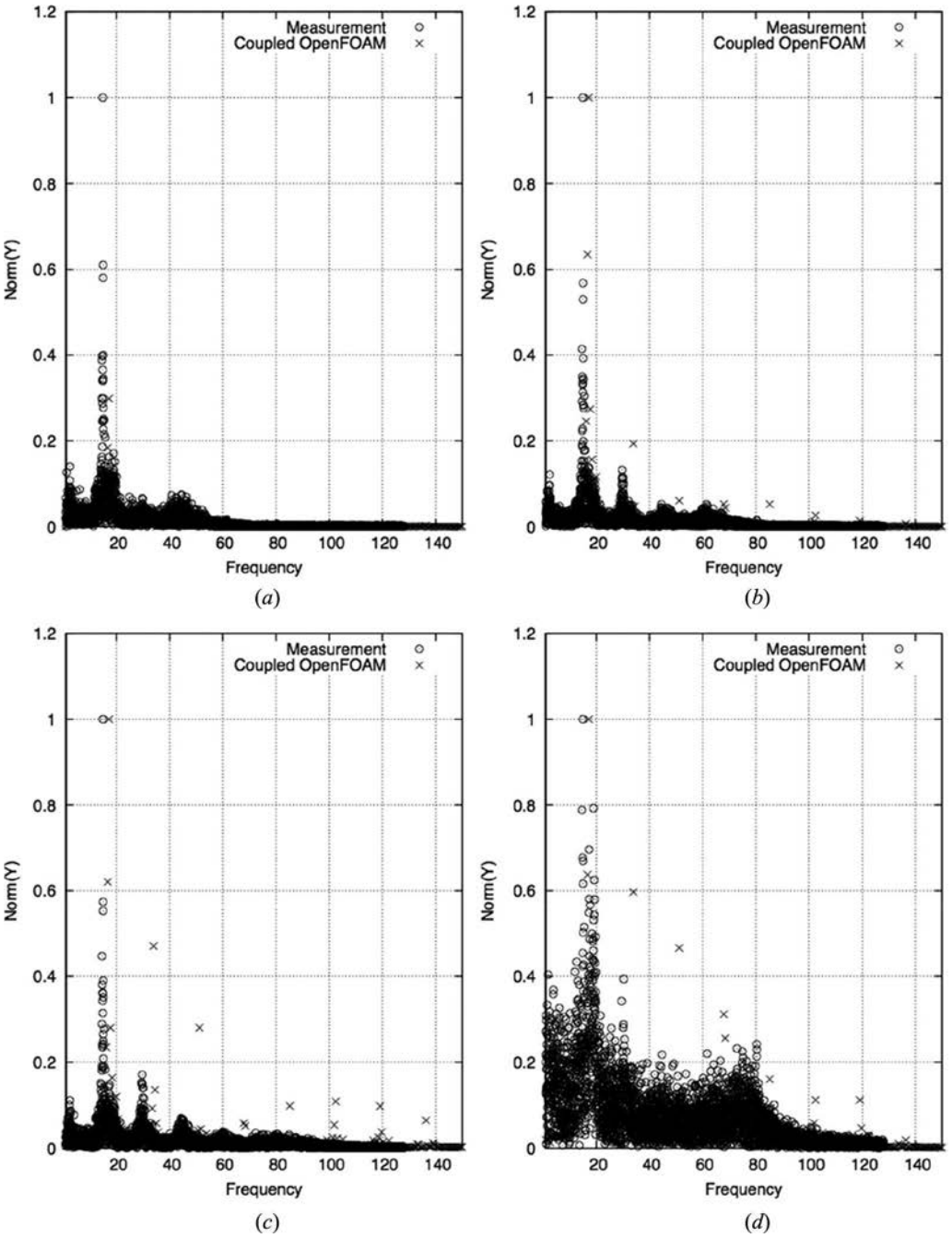

Figure 10. Comparison of the predicted and measured pressure signals at positions MG0, MG1, MG2, and MG3.

compared with the ones reported by Muntean et al. [23,24] who also judged CFD results against data for the same experimental setup. The good agreement in results demonstrates the capability of the coupled implicit ALE pressure-based algorithm to predict with good accuracy transient phenomena. Numerical results do not show any additional numerical dissipation resulting from the fully implicit treatment at non-matching multi-block interfaces suggesting that the developed ALE algorithm can be adopted with advantage in Reynolds Averaged Navier-Stokes (RANS) transient simualtions involving moving meshes.

Conclusion

A multi-block and fully coupled pressure-based transient flow solver implemented in OpenFOAM® was presented. The solver is capable of predicting incompressible turbulent flows in ALE formulation. The performance of the solver was evaluated by comparison with available experimental data of a swirl generator test case. Averaged numerically predicted meridional and tangential velocity profiles were found to be in good agreement with LDV measured profiles. The vortex rope's fundamental frequency was predicted rather accurately by the solver, given that it is a single phase flow algorithm and the vortex may contain a vaporous core. As reported by Petit et al. [22], more accurate results may also be achieved by refining the numerical time step.

The solver is robust, in the sense that during simulations no numerical crashes occurred, even when testing with very large time steps. Moreover, due to the implicit coupling, the inner iteration loops converged rapidly. Furthermore, the fully implicit discretization method at mesh interfaces implemented in this work had no negative effect on the convergence rate while guaranteeing conservation of fluxes at these interfaces.

Acknowledgments

The help of Sebastian Muntean (Polytechnic University of Timisoara) by providing the experimental data for the test case is gratefully acknowledged. The effort of the OpenFOAM Turbomachinery SIG (Olivier Petit) by providing the numerical setup for the test case is gratefully acknowledged.

Funding

The financial support granted by the Austrian research fund FFG for project 828688—HydroSim and project M 1543-N30 is gratefully acknowledged.

References

[1] L. Mangani, M. Buchmayr, and M. Darwish, Development of a Novel Fully Coupled Solver in OpenFOAM: Steady-State Incompressible Turbulent Flows, *Numer. Heat Transfer B Fund.*, vol. 66, pp. 1–20, 2014.
[2] L. Mangani, M. Buchmayr, and M. Darwish, Development of a Novel Fully Coupled Solver in OpenFOAM: Steady-state Incompressible Turbulent Flows in Rotational Reference Frames, *Numer. Heat Transfer B Fund.*, vol. 66, pp. 526–543, 2014.
[3] L. Mangani and M. Darwish Development of a Pressure Based Coupled CFD Solver for Turbulent, and Compressible Flows, *9th International OpenFOAM Workshop*, Zagreb, Croatia, June16–19, 2014.
[4] M. Darwish, M. Buchmayr, and L. Mangani, Development of a Coupled Free-Surface Solver in OpenFOAM *9th International OpenFOAM Workshop*, Zagreb, Croatia, June16–19, 2014.
[5] L. Mangani, M. Darwish, and F. Moukalled, An OpenFOAM Pressure-Based Coupled CFD Solver for Turbulent and Compressible Flows in Turbomachinery Applications, *Numer. Heat Transfer B Fund.*, vol. 69, no. 5, pp. 413–431, 2016.
[6] S. Patankar and D. Spalding, A Calculation Procedure for Heat Mass and Momentum Transfer in Three-Dimensional Parabolic Flows, *Heat Mass Transfer*, vol. 15, pp. 1787–1806, 1972.
[7] F. Moukalled and M. Darwish, A Unified Formulation of the Segregated Class of Algorithms for Fluid Flow at All Speeds, *Numer. Heat Transfer B Fund.*, vol. 37, no. 1, pp. 103–139, 2000.
[8] F. Moukalled and M. Darwish Pressure Based Algorithms for Single and Multifluid Flows, in W. J. Minkowycz, E. M. Sparrow, and J. Y. Murthy (eds.), *Handbook of Numerical Heat Transfer*, 2nd ed., pp. 325–367, Wiley, Hoboken, NJ, 2006.
[9] M. Darwish, W. Geahchan, and F. Moukalled, Fully Implicit Coupling for Non-Matching Grids *International Conference of Numerical Analysis and Applied Mathematics (ICNAAM 2010)*, Rhodes, pp. 47–50, 2010.
[10] M. Darwish, W. Geahchan, and F. Moukalled, A Fully Implicit Method for Coupling Multi-Block Meshes with Non-Matching Interface Grids, *Numer. Heat Transfer, Part B*, vol. 71, no. 2, pp. 109–132, 2017.
[11] F. Menter, M. Kuntz, and R. Langtry *Ten Years of Industrial Experience with the SST Turbulence Model*, pp. 625–632, Begell House, Inc., 2003.
[12] M. Buchmayr Development of Fully Implicit Block Coupled Solvers for Incompressible Transient Flows, Ph.D. thesis, Graz University of Technology, Graz, 2014.

[13] M. Darwish, I. Sraj, and F. Moukalled, A Coupled Finite Volume Solver for the Solution of Incompressible Flows on Unstructured Grids, *J. Comput. Phys*., vol. 28, no. 1, pp. 180–201, 2009.
[14] M. Darwish, I. Sraj, and F. Moukalled, A Coupled Incompressible Flow Solver on Structured Grids, *Numer. Heat Transfer B Fund*., vol. 52, pp. 353–371, 2007.
[15] F. Moukalled, A. Abdel Aziz, and M. Darwish, Performance Comparison of the NWF and DC Methods for Implementing High-Resolution Schemes in a Fully Coupled Incompressible Flow Solver, *Appl. Math. Comput*., vol. 217, no. 11, pp. 5041–5054, 2011.
[16] L. Mangani, M. Darwish, and F. Moukalled, An OpenFOAM Pressure-Based Coupled CFD Solver for Turbulent and Compressible Flows in Turbomachinery Applications, *Numer. Heat Transfer B Fund*., vol. 69, no. 5, pp. 413–431, 2016.
[17] M. Darwish and F. Moukalled, TVD Schemes for Unstructured Grids, *Int. J. Heat Mass Transfer*, vol. 46, pp. 599–611, 2003.
[18] C. Rhie and W. Chow, A Numerical Study of Turbulent Flow Past an Isolated Airfoil with Trailing Edge Separation, *AIAA J*., vol. 21, pp. 1525–1532, 1983.
[19] R. Susan-Resiga, and S. Muntean, Decelerated Swirling Flow Control in the Discharge Cone of Francis Turbines *Proceedings of the Fourth International Symposium on Fluid Machinery and Fluid Engineering*, Beijing, China, pp. 89–96, 2008.
[20] A. Bosioc, R. Susan-Risega, S. Muntean, and C. Tanasa, Unsteady Pressure Analysis of a Swirling Flow with Vortex Rope and Axial Water Injection in a Discharge Cone, *J. Fluids Eng*., vol. 134, p. 11, 2012.
[21] C. Tanasa, R. Susan-Risega, S. Muntean, and A. Bosioc, Flow-Feedback Method for Mitigating the Vortex Rope in Decelerated Swirling Flows, *J. Fluids Eng*., vol. 135, p. 11, 2013.
[22] O. Petit, A. Bosioc, H. Nilsson, S. Muntean, and R. Susan-Risega, Unsteady Simulation of the Flow in a Swirl Generator using Open-Foam, *Int. J. Fluid Mach. Syst*., vol. 4, pp. 199–208, 2011.
[23] S. Muntean, A. Bosioc, R. Stanciu, C. Tanasa, and R. Susan-Resiga, 3D Numerical Analysis of a Swirling Flow Generator, *Fourth International Meeting on Cavitation and Dynamic Problems in Hydraulic Machinery and Systems*, Belgrade, Serbia, 2011.
[24] S. Muntean, H. Nilsson, and R. Susan-Resiga, 3D Numerical Analysis of the Unsteady Turbulent Swirling Flow in a Conical Diffuser Using Fluent, and OpenFoam, *3rd IAHR International Meeting of the Workgroup on Cavitation and Dynamic Problems in Hydraulic Machinery and Systems*, October 14–16, Brno, Czech Republic, 2009.